JOURNAL OF THE ROYAL SOCIETY Interface

rsif.royalsocietypublishing.org

Research

Cite this article: Richards CT, Clemente CJ. 2013 Built for rowing: frog muscle is tuned to limb morphology to power swimming. J R Soc Interface 10: 20130236.
http://dx.doi.org/10.1098/rsif.2013.0236

Received: 13 March 2013
Accepted: 25 April 2013

Subject Areas:
biomechanics, biomimetics

Keywords:
muscle, power, rowing, swimming, frogs, robotics

Author for correspondence:
Christopher T. Richards
e-mail: richards@fas.harvard.edu

Electronic supplementary material is available at http://dx.doi.org/10.1098/rsif.2013.0236 or via http://rsif.royalsocietypublishing.org.

Royal Society Publishing
Informing the science of the future

Built for rowing: frog muscle is tuned to limb morphology to power swimming

Christopher T. Richards and Christofer J. Clemente

The Rowland Institute at Harvard, Harvard University, 100 Edwin H. Land Boulevard, Cambridge, MA 02142, USA

Rowing is demanding, in part, because drag on the oars increases as the square of their speed. Hence, as muscles shorten faster, their force capacity falls, whereas drag rises. How do frogs resolve this dilemma to swim rapidly? We predicted that shortening velocity cannot exceed a terminal velocity where muscle and fluid torques balance. This terminal velocity, which is below V_{max}, depends on gear ratio (GR = outlever/inlever) and webbed foot area. Perhaps such properties of swimmers are 'tuned', enabling shortening speeds of approximately $0.3V_{max}$ for maximal power. Predictions were tested using a 'musculo-robotic' *Xenopus laevis* foot driven either by a living *in vitro* or computational *in silico* plantaris longus muscle. Experiments verified predictions. Our principle finding is that GR ranges from 11.5 to 20 near the predicted optimum for rowing (GR $\approx$ 11). However, gearing influences muscle power more strongly than foot area. No single morphology is optimal for producing muscle power. Rather, the 'optimal' GR decreases with foot size, implying that rowing ability need not compromise jumping (and *vice versa*). Thus, despite our neglect of additional forces (e.g. added mass), our model predicts pairings of physiological and morphological properties to confer effective rowing. Beyond frogs, the model may apply across a range of size and complexity from aquatic insects to human-powered rowing.

1. Introduction

The study of spectacular frog jumps [1,2] has enriched our understanding of muscles [3] as well as muscle–tendon joint mechanics [4]. Less celebrated is their impressive swimming ability [5–7] which has revealed important mechanisms of fluid propulsion [8–10], making frogs ideal models to probe the limits of muscle-powered swimming.

From frog muscle studies, the principles of muscle contraction are well understood. As active muscle shortens, the available force rises then falls depending on overlap between thick and thin filaments as the muscle's operating length changes [11]. In addition, muscle force capacity decays to zero as contraction speed approaches maximum shortening velocity, V_{max} [12]. Along with time-dependent properties (such as rates of force rise and decay), these force–length and force–velocity (F–V) properties define the ceiling of force and power which muscle cannot exceed. Yet, independent from the familiar F–V property, fluid dynamics dictate that drag force is approximately proportional to approximately velocity^2. Hence, Daniel *et al.* [13] observed a dilemma: as muscle shortening velocity increases, force capacity falls owing to the F–V limitation while drag force rises steeply. Given this conflict between muscle versus fluid properties, how can a muscle move a limb rapidly for swimming?

We illustrate Daniel's dilemma with a hypothetical muscle moving a flat plate in water (figure 1). In this simple case where we neglect both added mass effects [13] and changes in fluid force orientation, drag is proportional to muscle shortening velocity $(V_m)^2$. Thus, F–V and drag curves can be superimposed. As the muscle contracts, the plate accelerates until drag balances the limiting force of the F–V curve where the curves intersect (point '*X*'). V_m cannot exceed *X* because drag force at faster speeds would exceed available muscle force, constraining the muscle to operate leftward of *X*. Furthermore,

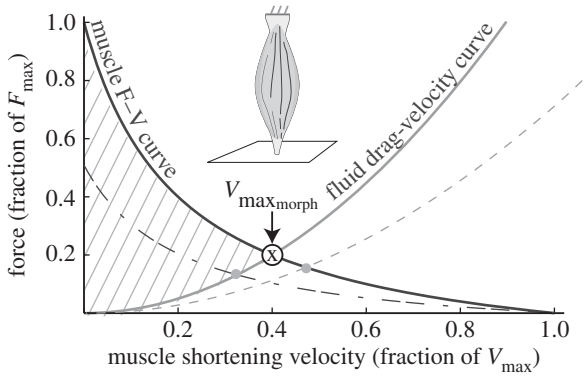

Figure 1. Daniel's dilemma [13]: the muscle force–velocity (F–V) curve (black) opposes the rising drag force (grey). A muscle moving a flat plate through water predicts that the intersection point ($V_{max_{morph}}$) limits shortening velocity because faster speeds incur drag forces above the F–V curve. Theoretically, muscle must operate both below the F–V curve and above the drag curve (hatched region) since the muscle must generate at least enough force to overcome drag. The current study predicts that decreasing plate area decreases drag, shifting $V_{max_{morph}}$ rightward (dashed). Decreasing muscle cross-sectional area (lowering maximum force) shifts $V_{max_{morph}}$ leftward (dashed-dotted).

both muscle properties (physiological cross-sectional area 'PCSA' and V_{max}) as well as plate morphology influence the location of point *X*. For example, decreasing the plate area lowers the drag force at any given velocity, thus shifting *X* rightward (dashed line, figure 1). Reciprocally, decreasing PCSA lowers maximum muscle force, shifting *X* leftward (dashed-dotted line, figure 1). Hence, we name *X* the 'morphological V_{max} ($V_{max_{morph}}$)' because both the morphology of the muscle and of the plate determine the maximum V_m, regardless of the physiological V_{max}.

In light of $V_{max_{morph}}$, we attempt to resolve Daniel's dilemma. Because muscle power (force × velocity) peaks at approximately $1/3V_{max}$ we expect $V_{max_{morph}} \approx 0.3V_{max}$ for rapid swimming. We consider *Xenopus laevis*, an obligatorily aquatic frog which catches prey and avoids predators [14] using webbed foot rowing. The plantaris longus (PL) in *X. laevis* attaches to a lever rotating a joint at a distance *r* (inlever; figure 2) to generate propulsive drag at an outlever distance, *R*. The resulting joint rotation causes tangential velocity (velocity tangent to the foot's arc rotating about the ankle joint) creating propulsive fluid reaction force which is a function of gear ratio ('GR' = R/r). Since drag is proportional tangential velocity^2 (=$R^2 \cdot$ joint angular velocity^2), drag owing to muscle shortening rises with GR. Knowing that drag is a major component of the fluid force acting on *X. laevis* feet [15], we can analytically demonstrate that $V_{max_{morph}}$ decreases with GR because increasing GR raises the muscle force required to move a given load [16,17]. Moreover, foot area increases drag, therefore, will decrease $V_{max_{morph}}$. Therefore, since muscle power peaks at approximately $1/3V_{max}$ [3], increases in foot area (or GR) will either increase or decrease muscle power, depending on whether $V_{max_{morph}}$ lies above or below $1/3V_{max}$, respectively. Thus, we predict that *X. laevis* hindlimb morphology (GR and area) is 'tuned' to the muscle intrinsic properties to maximize muscle power output. Using the PL from *X. laevis*, we derived analytical predictions that were then verified using a 'musculo-robotic' frog foot [18].

2. Material and methods

2.1. The analytical model

Based upon recent models [19,20], we assumed that muscle F–V properties dominate muscle function in frog swimming. For a rigid, flat, fin rotating at 90° angle-of-incidence, we expressed hydrodynamic thrust in terms of inertia, muscle contractile properties, gearing and fin size. Equations were modified from earlier work [20]. Inertial torque on the foot is the difference of muscle torque and drag torque,

$$I \cdot \ddot{\theta} = F_{muscle} \times r - F_{drag} \times R, \tag{2.1}$$

where *I* is the system moment of inertia (see below), and θ is the anterior–posterior foot angle with respect to the body midline (i.e. 0° points to the forward direction of swimming). The inlever is *r* and the outlever is *R* (figure 2). Note that because the orientation of the F_{drag} vector can change through time, *R* can also be time-varying (see §4). Drag torque is

$$R \cdot \frac{1}{2} \cdot C_D \cdot A_{fin} \cdot \rho \cdot \left(\frac{d\theta}{dt} R + v_{backward} + v_{COM} \right)^2, \tag{2.2}$$

where C_D is the foot drag coefficient (=2 for this study; [15]), A_{fin} is the fin surface area, ρ is water density. $R \cdot d\theta/dt$ is the tangential rotational velocity vector normal to the foot surface. Translational velocity terms represent the backward push of the legs relative to the body ($v_{backward}$) and the forward motion of the centre of mass (v_{COM}) [8]. Note, the fluid force vector is normal to the foot with pure rotational motion, however when translational motion is substantial, the vector deviates from normal (see §4). For an initial kick of *X. laveis* from rest, translational terms nearly cancel [15], leaving drag only a function of tangential rotational velocity^2. Thus, in our simple analytical model, we neglect translational velocity (see §4). For our rotational model, the inertial torque is the sum of the foot's moment of inertia (I_{foot}) and the added mass torque, each calculated about the centre of foot rotation,

$$I = I_{foot} + M_{66} \cdot \ddot{\theta}, \tag{2.3}$$

where M_{ij} is the 6 × 6 added mass coefficient matrix describing *j* force components caused by *i* velocity components which vary depending on orientation and shape of the foot. M_{66} is the purely rotational added mass coefficient. Translational terms introduce substantially more complex equations which have been previously described [15]. For our simple analytical model, we exclude added mass (see below).

For the PL muscle, we considered a simplified Hill-type muscle model,

$$F_{muscle} = \mathrm{Act}(t) \cdot \mathrm{FV}(t) \cdot \mathrm{FL}(t), \tag{2.4}$$

where Act(*t*) is the time-varying activation of the muscle (representing both the active state as well as the maximum isometric force) and FV(*t*) and FL(*t*) (see equation (2.10)) are time-varying gain functions signifying the contributions of F–V and F–L effects. As we aim to model peak muscle performance, we assume FL = 1 and Act = maximum, assuming that a muscle should reach maximum activation at L_o, the plateau of the F–L curve. This is a valid assumption for frogs given their ability to begin muscle contractions at long lengths (starting length > L_o) such that they reach L_o at peak activation ([21,22]; i.e. FL = 1 at maximum activation). If starting length were to vary significantly, our exclusion of F–L properties would be invalid (see §4). Thus, we estimate the muscle force limit

$$\approx \text{maximum Act} \cdot \mathrm{FV} = 20 \cdot \mathrm{PCSA} \cdot \mathrm{FV}, \tag{2.5}$$

with peak isometric stress = 20 N cm^{-2} and PCSA = 0.3 cm^2 [23], giving a maximum force of 6 N at peak activation. The

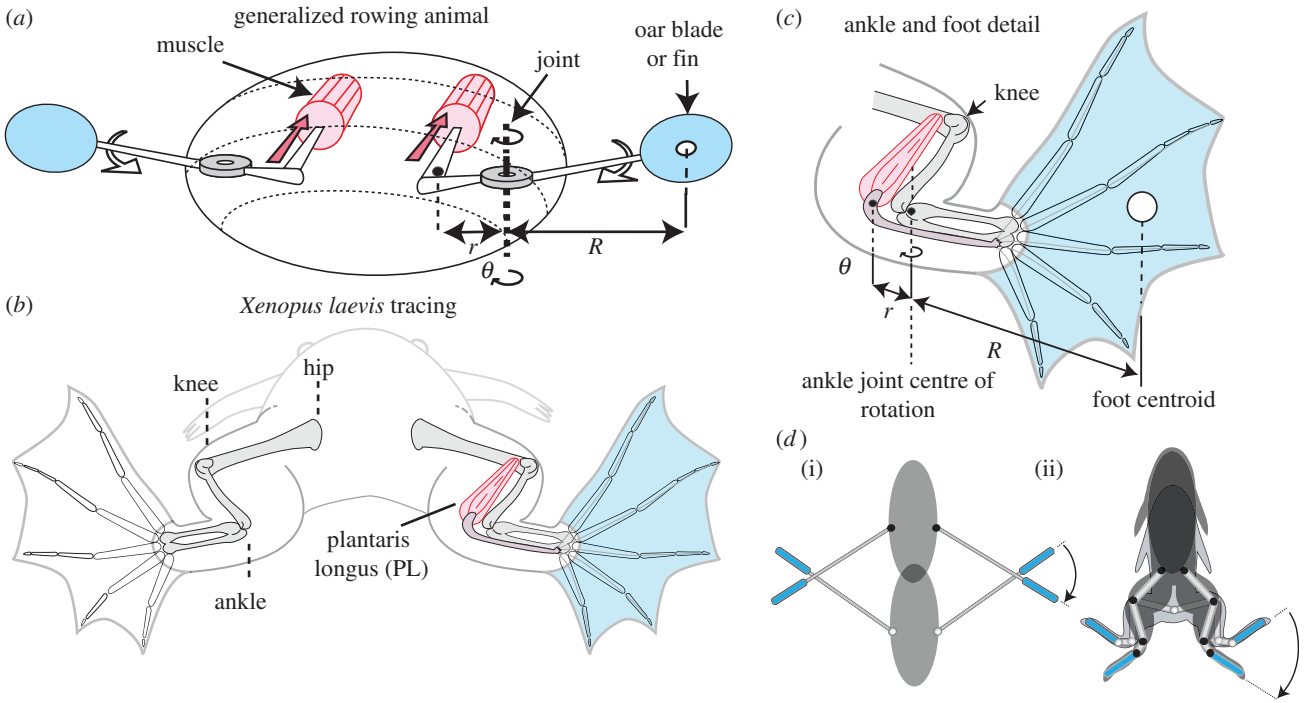

Figure 2. Anatomy of a hypothetical animal rower (*a*) showing a pair of rowing appendages that rotate about an angle (θ) driven by muscles contracting against an inlever (r). Propulsive drag arises at the end of the outlever (R). A tracing of *Xenopus laevis* (*b*) shows the PL muscle as the main motor for swimming. A sketch of the lower limb (*c*) shows how r and R are defined with respect to the ankle joint. Schematic diagrams (*d*) of a notonectid insect (i) and a frog (ii) illustrate how the oars rotate with respect to the water as the body moves forward.

F–V curve was fitted from the following equation [18]:

$$\mathrm{FV}(t) = \frac{2.61 - V_\mathrm{m}(t) \cdot 2.61/v_\mathrm{max}}{V_\mathrm{m}(t) + 2.61}, \quad V(t) \geq 0, \tag{2.6}$$

where average $V_\mathrm{max} \approx 8$ [22]. Since drag forces dominate in *X. laevis* swimming [15], we assumed peak fluid force occurs when drag is maximum (i.e. at peak rotational velocity and rotational acceleration = 0). Thus, at peak fluid force, we ignore added mass effects (although they are included in the physical model experiments below). Finally, for small angular changes

$$\frac{\mathrm{d}\theta}{\mathrm{d}t} \approx \frac{V_\mathrm{m}}{r}. \tag{2.7}$$

Substituting $\mathrm{GR} = R/r$ into equation (2.2) given the torque balance at 0 acceleration equation (2.1), we obtain

$$F_\mathrm{muscle} = 20 \cdot \mathrm{PCSA}\left(\frac{2.61 - V_\mathrm{m}(t) \cdot 2.61/v_\mathrm{max}}{V_\mathrm{m}(t) + 2.61}\right), \quad \text{at } V_\mathrm{m} = V_{\mathrm{max}_\mathrm{morph}} \tag{2.8}$$

and

$$F_\mathrm{drag} = \mathrm{GR} \cdot \tfrac{1}{2} C_\mathrm{D} A_\mathrm{fin} \rho \cdot (\mathrm{GR} \cdot l_\mathrm{rest} V_\mathrm{m})^2, \quad \text{at } V_\mathrm{m} = V_{\mathrm{max}_\mathrm{morph}} \tag{2.9}$$

where PCSA is in cm^2 and V_m is in terms of muscle lengths s^{-1} ($\mathrm{ML\,s}^{-1}$) and l_rest is the resting muscle length. $V_{\mathrm{max}_\mathrm{morph}}$ is found either by setting equation (2.8) = equation (2.9) or by plotting the curves and finding the intersection point. Note that our simplified model assumes that maximum activation occurs nearly simultaneous with the peak of the FL curve (see §4).

2.2. Musculo-robotic experiments

Predictions from the analytical model were tested with a bio-robotic setup (see the electronic supplementary material, figure S1) that was recently described [18]. Briefly, circular rigid plexiglass feet were mounted to a rotating servo motor resting above an aquarium. Three foot areas were chosen (areas = 2, 5 and 10 cm^2) corresponding to 0.4×, 1× and 2× natural *X. laevis* foot area. The motor was controlled either by a living muscle isolated *in vitro* (*in vitro-robotic* method) or by a computational model simulating the behaviour of a Hill-type muscle (*in silico-robotic* method). For *in vitro-robotic* experiments, PL muscle was removed from the animal and mounted to a 305C-LR servo ergometer (Aurora Scientific, Inc., Aurora, Ontario, Canada) as described previously [23]. The muscle was stimulated supramaximally with a 80 ms train of 1 ms pulses at 250 Hz using parallel stainless steel plate electrodes. Using a 'real-time' platform (cRio9074 FPGA controller, National Instruments, Austin, TX, USA), force recoded from the muscle was multiplied by a virtual inlever, r, and applied as a torque command signal to the robotic foot. Following a 0.1 ms feedback delay, displacement of the robotic foot was then relayed back to the ergometer enabling the muscle to shorten as if actuating the robotic fin directly. For *in silico-robotic* experiments, the computational model was fed an activation waveform output (see below) from a USB-6289 A/D module (National Instruments). In the real-time controller, position data from the motor were monitored and input into F–V and F–L equations to compute force at the next 0.1 ms time step. Force was converted to torque via r in software. For both *in vitro* or *in silico* experiments, R was assumed to be the constant distance between the motor centre of rotation and the foot centroid, and GR could be controlled by changing r in software. Although F–L properties were excluded from the simple analytical model, experimental trials included both F–L and F–V curves. Consequently, the robotic foot behaves as an ankle joint actuated by a simplified Hill-type model (equation (2.4)) with F–V properties (described above) and the following F–L equation [22,24]:

$$\mathrm{FL}(t) = \mathrm{e}^{-|((\mathrm{L}/\mathrm{L_o})^b - 1)/s|^a}, \tag{2.10}$$

where $\mathrm{L/L_o}$ = instantaneous length/optimal length, $b = -2.53$, $s = -0.59$ and $a = 1.41$. Activation dynamics were simulated by inputting a train of spikes (identical to the stimulation used for *in vitro-robotic* experiments) into a three-stage activation equation [25]

$$\frac{\mathrm{d}}{\mathrm{d}t} a_i = \frac{1}{\tau_i} a_{i-1} - \left[\frac{a_i}{\tau_i}[\beta_i + (1 - \beta_i) a_{i-1}]\right] \tag{2.11}$$

Table 1. Summary of simplifying assumptions made in the analytical versus experimental approaches used.

property included	analytical model	musculo-robotic experiments (*in silico-robotic* and *in vitro-robotic*)
muscle activation dynamics	absent	present
muscle force–length effects	absent	present
muscle force–velocity effects	present	present
fluid added mass effects	absent	present
fluid drag effects	present	present

$$\boldsymbol{\tau}_{1,2,3} = \{19.75, 0.44, 23.62\}, \quad \boldsymbol{\beta}_{1,2,3} = \{0.92, 0.08, 0.96\},$$

where i is the activation stage (i from 1 to 3), a_{i-1} is the activation waveform from the previous stage, a_0 is the input waveform of spikes and a_3 is the output muscle active state, Act, used to simulate muscle force (equation (2.4)). Values of $\boldsymbol{\tau}$ and $\boldsymbol{\beta}$ were obtained using a genetic algorithm [26] in LabVIEW 2011 (National Instruments) to match both twitch and tetanic force profiles from isometric contractions of the *X. laevis* PL. To minimize confounding FL effects, for each *in silico-robotic* trial, muscle starting length was adjusted between 1.0 and 1.26 to enable peak activation to coincide with peak force [22]. Given the simplifying assumptions of our above analytical model (table 1), *in silico-robotic* and *in vitro-robotic* experiments were used for verification.

Hydrodynamic force was measured from strain gauges mounted to a custom-built sensor attached at the base of the robotic foot (see [18] for details). The force signal was amplified using a model 2120 amplifier (Vishay Intertechnology, Inc., Malvern, PA, USA). All signals were recorded using a National Instruments A/D board (USB-6289).

2.3. Estimating *in vivo* gear ratios

Estimates for GRs were from small adult male *X. laevis* frogs (28.59 ± 4.34 g mean $\pm$ s.d. body mass; $N = 5$). The PL inlever, r, value of 0.14 cm was obtained from the tendon travel technique [27]. To calculate R, the foot centroid was located from digital tracings of photographs of the feet (ImageJ, U.S. National Institutes of Health, Bethesda, MD, USA). R was estimated at 'mid-stroke' (foot angle $= 90^\circ$ to flow). Using joint kinematics data [15], a line was drawn normal to the foot originating at the centroid. R was calculated as the perpendicular distance between the drawn line and the ankle joint at mid-stroke.

3. Results

3.1. Morphological $V_{max_{morph}}$ predictions from the model compared with *in vivo* data

For a 5 cm^2 foot (similar to the size of a *X. laevis* foot), the model predicted drag force curves of increasing steepness as GR varied from 5 to 17 (figure 3*a*). $V_{max_{morph}}$ decreased from 5.2–3.3 to 2.3–1.7 muscle lengths s^{-1} (ML s^{-1}). Similarly, increasing foot area from 2 to 10 cm^2 (at GR = 13) caused $V_{max_{morph}}$ to decrease from 3.1 to 1.8 ML s^{-1}. Increasing either GR or area also caused power to increase then decrease as $V_{max_{morph}}$ shifted towards then away from $1/3V_{max}$. For any given relative muscle area (muscle PCSA/foot area), both muscle power and hydrodynamic force rise and fall about an 'optimal' GR value. This optimal GR was predicted to shift rightward as relative muscle area increases (figure 3*b*,*c*). From this theoretical performance map, the GR of the *X. laevis* PL (relative area = 0.3 cm^2/5 cm^2 = 0.06) was predicted to be approximately 11. Near this predicted maximum muscle power and fluid force, estimates of *in vivo* GR ranged from 11.5 to 20, measured at different points of the foot stroke and GR $\approx$ 18 at mid-stroke.

3.2. Musculo-robotic measurements of morphological V_{max}

Following electrical stimulation, *in vitro* muscle force developed in response to hydrodynamic force (figure 4). Since experiments to determine the F–V curve could not be performed on the same muscle preparations as *in vitro-robotic* trials, $V_{max_{morph}}$ could not be found precisely. However, the data clearly show muscle force and velocity increasing until reaching a maximum velocity near the predicted range of $V_{max_{morph}}$ (figure 5*a*). As GR increased from 5 to 11 to 17, the operating range of the muscle also shifted leftward, as predicted by the superimposed drag curves from the model. To more precisely test predictions of $V_{max_{morph}}$, *in silico-robotic* experiments were performed. Similar to *in vitro-robotic* trials, both force and velocity increased rapidly until near the point of maximum activation, at which time muscle force reached the limit imposed by the F–V curve (figure 5*b*). Plots of force versus velocity intercepted with the F–V curve near the predicted values of $V_{max_{morph}}$. Reflecting *in vitro-robotic* experiments, increasing GR compressed the muscle velocity range (i.e. approx. 0–5 MLs versus approx. 0–1.8 for GR = 5 versus 17). Although the analytical model predicted muscle force and velocity values to only occur above the drag force curve, both *in vitro* and *in silico* data fell below the drag curves during the relaxation phase of the muscle. This underestimate could be due to (i) slight deviations of the fluid reaction force vector causing lower outlever values than estimated by our model (see §4) or (ii) backward-directed force caused by added mass effects which counteract fluid drag late in the swimming stroke [15]. Consequently, $V_{max_{morph}}$ slightly underestimated actual peak V_m values.

3.3. Bio-robotic measurements of muscle power and hydrodynamic force

Relative peak muscle power (peak trial power relative to the maximum value observed) and hydrodynamic force were tested over a range of GR and foot sizes. For foot sizes of 2, 5 and 10 cm^2, the analytical model predicted maximum power and hydrodynamic force to occur at GR = 9, 11.4 and 15,

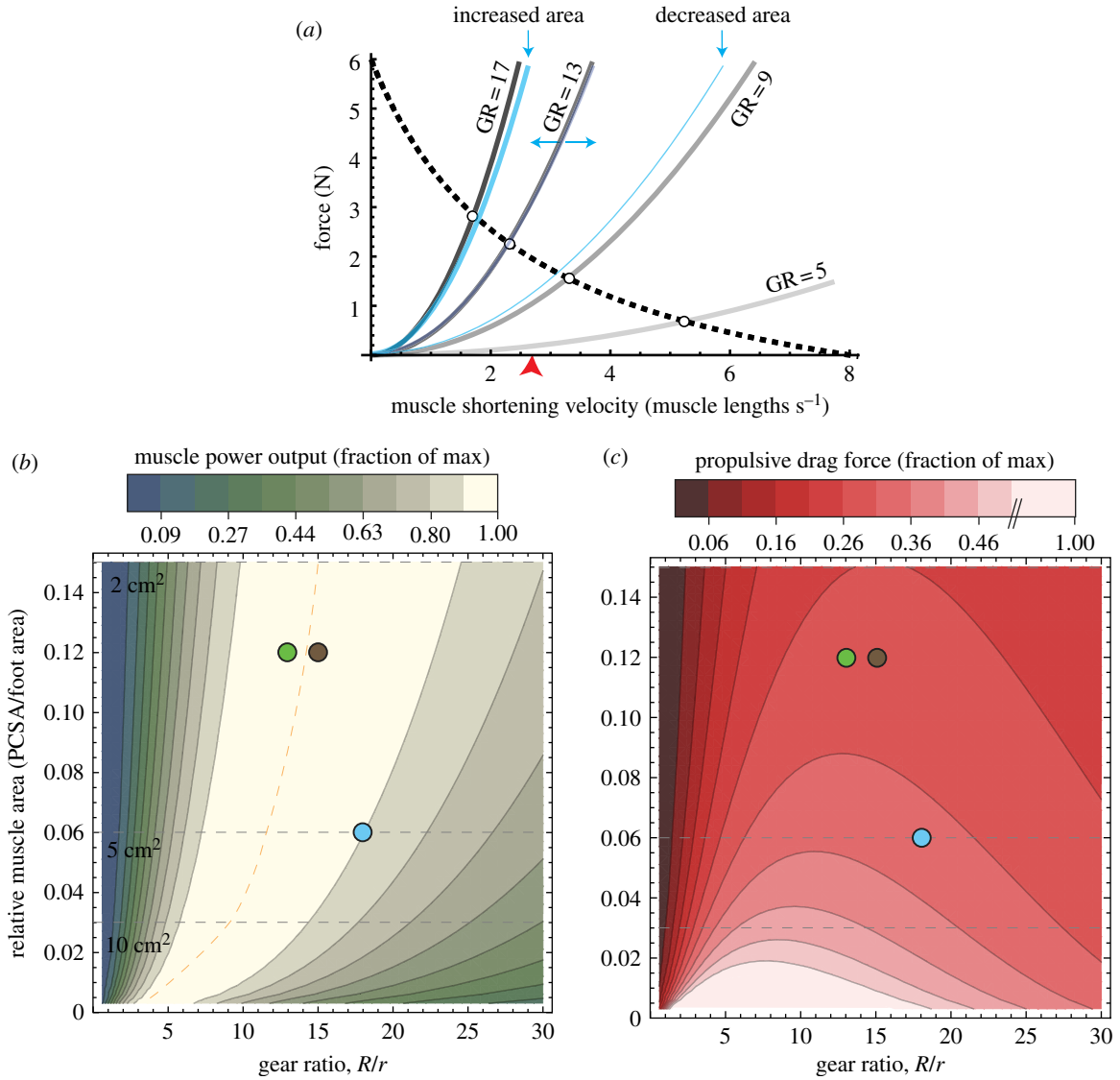

Figure 3. (*a*) The force–velocity curve for *Xenopus laevis* (black, dashed) is plotted against fluid drag (grey, solid) predicted for a foot area of 5 cm^2 (typical for *X. laevis*) at gear ratios (GR) of 5, 9, 13 and 17. Blue lines indicate the leftward or rightward shifts due to a foot area increase (10 cm^2) or decrease (2 cm^2) at GR = 13, respectively. Note how increases in either GR or foot area are predicted to compress the muscle's operating range. The red arrow indicates maximum power at 1/3V_{max}. (*b*) A theoretical map of muscle power output and (*c*) propulsive drag force show how 'optimal' GR depends on relative muscle area (and *vice versa*). Dotted grey lines predict values for foot areas of 2, 5 and 10 cm^2 tested with *in silico-robotic* experiments. Dots represent GR versus relative area values for example aquatic (*X. laevis*, blue) and semi-aquatic species (*Rana pipiens*, brown; *Rana catesbeiana*, green) at mid-stroke. Semi-aquatic species values were estimated from previous literature (see §2).

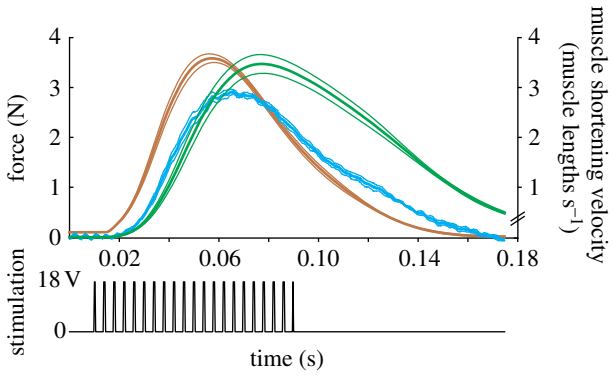

Figure 4. Traces of living *in vitro-robotic* muscle force (brown), shortening velocity (green), hydrodynamic force × 10 (blue) and muscle stimulation pulses (black) for GR = 11 (the predicted optimal value), foot area = 5 cm^2. Thick lines are mean and thin are standard deviation for $N = 3$ frogs.

respectively (figure 3*b*,*c*). In close agreement with theoretical predictions, *in silico-robotic* tests revealed that GR = 9, 11 and 13 for maximum peak muscle power (figure 6*a*) and GR = 9, 11 and approximately 11–15 for maximum peak hydrodynamic force (figure 6*b*).

4. Discussion

4.1. Optimal gear ratio for muscle power output can be predicted from limb morphology

During locomotion, muscle power output may be limited by its coupling to the load, rather than by intrinsic muscle properties. Because muscle power output correlates with swimming speed and acceleration [28] power likely limits performance. Aiming

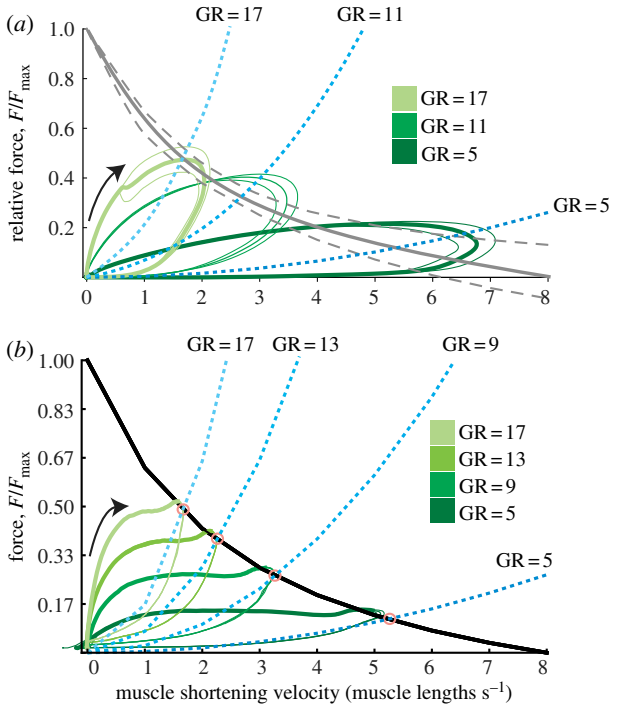

Figure 5. Force versus velocity plots for (*a*) *in vitro-robotic* and (*b*) *in silico-robotic* experiments. Grey curves are F–V curves. Dotted grey lines are 95% confidence bands representing uncertainty of matching *in vitro-robotic* data with F–V curves from separate experiments. Drag curves (blue, dotted) predict the diminishing operating range of the muscle as GR increases. Bold lines are mean and thin are standard deviation ($N = 3$ frogs or $N = 3$ replicates for *in vitro-robotic* or *in silico-robotic* trials, respectively). For *in silico* trials, thick lines represent data prior to peak muscle activation.

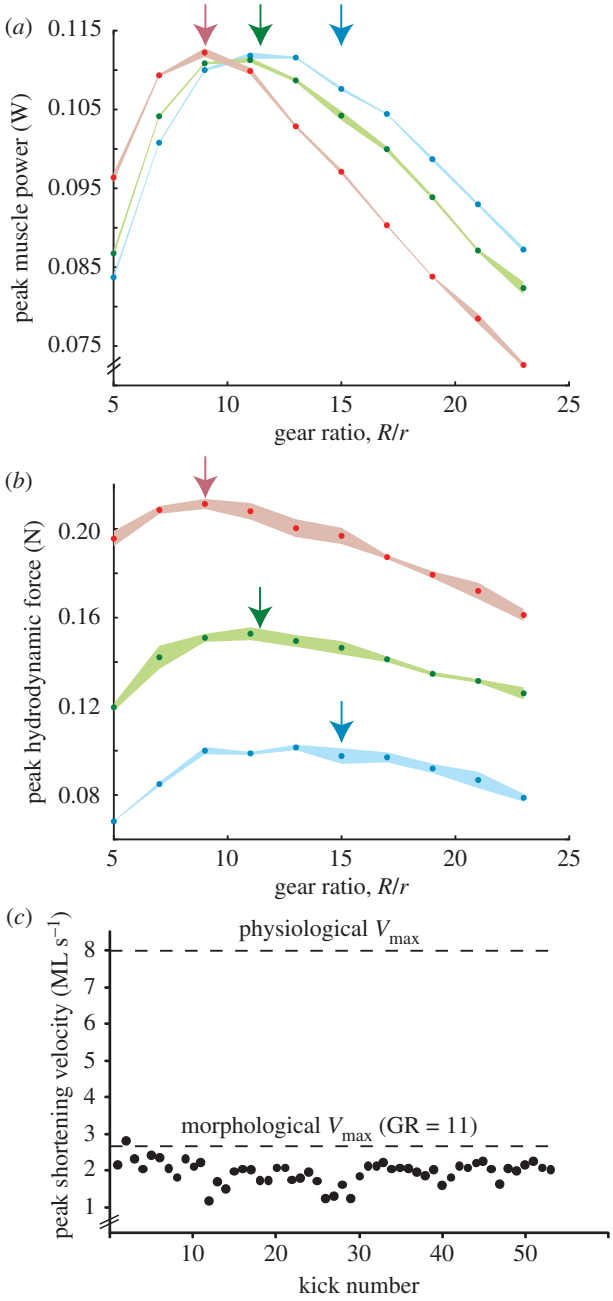

Figure 6. (*a*) Peak muscle power and (*b*) peak hydrodynamic force for GR = 5, 7, 9, 11, 13, 15, 17, 21 and 23 tested using circular foot sizes of 2 (blue), 5 (green) and 10 cm^2 (red). Arrows show analytically predicted locations of maxima (along dotted grey lines of contour plots; figure 3*b*,*c*). Dots are mean values and shaded areas are $\pm$ standard deviation for $N = 3$ replicates. Muscle starting length was adjusted so that peak force coincided with peak activation (see §2). (*c*) Peak *in vivo* PL muscle shortening velocity during *X. laevis* swimming [28].

to explore conditions under which power is 'optimized' (i.e. shortening velocity $\approx 1/3V_{max}$), we developed a predictive model that was tested using recent musculo-robotic tools. As predicted, results from both the analytical model and experimental trials suggest that aquatic frog physiological and limb morphological properties may be tuned for swimming. Findings also suggest that there need not be a trade-off between swimming and jumping ability.

Our analytical model, despite its simplicity, accurately predicted how changes in external morphology (e.g. foot area) and in internal morphology (e.g. joint gear ratio, 'GR') limit muscle power. Simple analysis reveals that drag force experienced by the muscle is proportional to $A_{fin} \times GR^3$ (equation (2.9)). Thus, we expected slower contraction speeds (lower $V_{max_{morph}}$) owing to increases in either GR or foot area, as demonstrated by our experimental data (figure 5). In addition, as expected, increases in GR caused peak muscle power to rise and fall as $V_{max_{morph}}$ approached then regressed from $1/3V_{max}$. More broadly, current findings suggest that for high Reynolds number rowing, the limits to muscle power and hydrodynamic force can be predicted as a simple function of muscle area relative to foot area (relative area = PCSA/foot area) and GR. Consequently, our analytical model reveals two general strategies for maximizing muscle power against a fluid load: (i) high gear with large relative muscle area (e.g. large muscle, small fin) or (ii) low gear with small relative muscle area (e.g. small muscle, large fin). Specifically, larger feet (smaller relative muscle area) require lower GR to maintain a given power output against a fluid load, whereas small feet (large relative muscle area) would not be sufficiently loaded if the GR were too low. *Xenopus laevis* frogs, for example, have larger fin areas and smaller PL PCSA than *Rana pipiens* or *Rana catesbeiana* of similar body mass (relative area = 0.06 versus 0.12; (this study, [4,21,29–31]). From these interspecific morphological differences, our model predicts *X. laevis* to operate at slightly lower gears (GR = 11) than ranid frogs (GR = 14). Consistent with model predictions, GR measurements of *X. laevis* ranged from 11 to 20 (depending on limb kinematics) and estimated GR values from previous literature [4,21, 29–31] for *R. pipiens* and *R. catesbeiana* were GR $\approx$ 15 and 13, respectively (figure 3*b*). However, because GR varies

in vivo (see below), these species are all likely to operate over a similar gearing range.

4.2. Estimated morphological V_{max} predicts maximum *in vivo* shortening velocity in *Xenopus laevis*

In addition to exploring how limb morphology might be tuned for rowing, our current findings have important implications on our understanding of *in vivo* muscle data. In traditional approaches to dynamic muscle function, one might use *in vitro* work loops [32,33] to address whether *in vivo* muscle operates at or near its intrinsic power limits. For example, some muscles may produce less power *in vivo* compared with their intrinsic potential measured *in vitro* [34]. However, muscle physiological approaches do not explain *why* muscle power output may be submaximal *in vivo*. Our current model predicts that if muscle contractile properties are not matched to the surrounding fluid via appropriate limb morphology, a muscle will operate below its power limits. Knowing that *X. laevis* operates at a minimum GR of approximately 11, shortening velocity should not exceed the $V_{max_{morph}}$ of approximately 2.7 ML s^{-1}. Data from experiments performed previously [28] show that *in vivo* PL shortening velocity remains below the predicted limit of approximately 2.7 ML s^{-1} (figure 6*c*). The match between $V_{max_{morph}}$ predictions and *in vivo* data suggests three points: (i) the PL is velocity-limited during swimming, (ii) the maximum contractile velocities observed *in vivo* approach $0.3V_{max}$ which is optimal for power generation, and (iii) *in vitro* work loop experiments performed above the $V_{max_{morph}}$ would produce results that are not physiologically possible for the muscle *in vivo*.

4.3. Jumping frogs may also possess morphological tuning for rowing at no expense to jumping performance

Armed with an understanding of how fluid loading may limit *in vivo* muscle function, we describe how the current model can be applied to address questions of comparative functional morphology. We illustrate the applications of the model by an analogy to human-powered rowing. Hypothetically, the rower represents a muscle which must operate within intrinsic speed and strength limits. The oar blade and oar lock represent the webbed foot and limb joint, respectively, whose gearing is determined by the inboard and outboard oar lengths (i.e. 'rigging'). Finally, the rules and regulations of the rowing sport represent functional constraints which may, for example, constrain the size of the oar blade. Knowing the strength and speed capacities of the rower, one should be able to predict the appropriate rigging to match the capabilities of a particular rower to optimize muscular power output.

Given the relationship between rowing ability, limb morphology and muscle properties, our model could be used to address morphological trade-offs between swimming and other locomotor tasks. Frog jumping ability [1,2] correlates to modifications of the skeleton [35], potentially in conflict with swimming. However, morphology of ranids (jumper–swimmers; [36]) and swimming performance of ranids versus pipids (swimmers; [37]) reveal no evidence that jumping diminishes swimming capacity. How can the musculoskeletal system excel both at swimming and jumping? The map of muscle power versus GR and relative area (figure 3*b*) suggests that there exist multiple combinations of foot size and GR which maximize muscle power. This broad 'solution space' perhaps could accommodate specializations for jumping while maintaining swimming ability (or vice versa). For instance, the recoil of elastic tendons to amplify muscle–tendon power output for jumping [4] requires appropriate tuning of GR to body mass [38], suggesting that jumping requirements may constrain GR. In such cases, changes in foot area could compensate (i.e. moving vertically along the power map). Alternatively, foot area may be constrained due to shorter feet. Large forces during jumping [4,10] may limit foot length in order to minimize joint torques. Indeed, the feet of hylid frogs, the champion jumpers, are short despite their elongated total hindlimb length relative to fully aquatic species [35]. In this case, adjustments of GR can move the limb horizontally along the power map to optimize power when faced with a foot area constraint. Thus, we speculate that due to the many pairings of GR and foot area that confer power output during swimming, there need not be a swimming–jumping trade-off—a 'specialized' jumper may still be morphologically tuned to optimize power during rowing. Further modelling would be necessary to address the consequences of morphological constraints on swimming versus jumping.

4.4. Variation in V_{max} probably influences the 'optimal' limb morphology for rowing

In addition to the morphological predictors of muscle performance, physiological properties such as V_{max} influence the relationship between limb morphology and power output. Specifically, increasing or decreasing V_{max} causes a leftward or rightward shift of the entire power map, respectively. For ectothermic animals such as anurans, large fluctuations in environmental temperature (either seasonally or with climate change [39]) would influence V_{max}, affecting where muscles operate on the FV curve. V_{max} in *X. laevis* increases with temperature ($V_{max} \approx 0.004 \times \text{temperature}^2 + 0.11 \times \text{temperature} + 2.5$ ML s^{-1}; [40]). Given that *X. laevis* swim to catch active prey and escape predators [14], climate fluctuations might influence their ecological success. Yet, the invasive population of *X. laevis* of the Santa Clara River (CA, USA) thrive year-round [14], despite average daily temperature fluctuations from approximately 7 to 24°C [41]. At the higher temperature extreme, the PL muscle functions slightly rightward of the predicted optimum (figure 3*b*). However during winter, V_{max} may drop to approximately 3.7 ML s^{-1}, causing a rightward shift in peak GR from 11.4 to 18. Consequently, the PL produces approximately 90 per cent of its maximum power during warm months and approximately 100 per cent of its potential power (given the depressed V_{max}) during colder months. Thus, although colder temperatures depress absolute muscle power, the rightward shift of the power map might enable muscles to use their full power potential at that given temperature by maintaining the muscle's ability to operate at approximately $1/3V_{max}$. Alternatively, if *X. laevis* limbs were to operate leftward the predicted peak power (GR < 11), falling temperatures would further reduce performance. For example, if *X. laevis* operated at GR = 9, it would produce approximately 98 per cent of its maximum power at 22°C, but only approximately 70 per cent at 7°C. In addition to low temperature effects, power would likely also be depressed at higher temperatures (despite greater V_{max}) owing to a rightward shift away from the optimum GR

measured at laboratory temperature (22°C). Perhaps the right-shift of the power map could explain the depressed swimming performance of *Xenopus* at high temperatures [39]. One should note however, that beyond our simple model, animals might also respond to temperature changes by modifying stroke kinematics or the dynamic shape of their feet. Regardless, such influences of temperature imply that limb morphology of birds and mammals might be more tightly tuned, given that their V_{max} would remain constant at their physiologically regulated temperature.

Using published V_{max} data, one also can make broad taxonomic comparisons among high Reynold's number rowers. For example, notonectid insects swim using a slow muscle (V_{max} approx. 1 ML s^{-1}; [20]) compared with frogs ($V_{max} \sim 9$). Consequently for notonectids, we see a very high GR (approx. 40) given both the rightward-shifted $V_{max_{morph}}$ and their small rowing appendage. By contrast, aquatic bird and mammal muscles operate at higher physiological temperatures, causing V_{max} to be higher [42], perhaps requiring relatively lower GR values. This requires further investigation.

4.5. Simplifying assumptions of the current model are appropriate for certain cases of aquatic locomotion, but not for others

Our model is simple, thus has physiological and morphological limitations which must be addressed. The most evident morphological simplification is the neglect of leg joints proximal to the ankle. We justify this simplification for *X. laevis* where ankle rotation produces most of the thrust. However, ranids rely considerably less on their ankle joint (producing approx. 50% of total thrust; [37]). Nevertheless, even in ranids, both ankle rotation and ankle stabilization (to maintain the foot's position as the proximal joints push backward) require great amounts of power produced at the ankle, justifying our model's focus on distal rather than proximal joints. Regardless of the model's simplicity, identical principles of $V_{max_{morph}}$ tuning would apply to more complex future models. In terms of the physiological simplifications, the interactions among F–V and F–L effects are potentially confounding given that large length changes reduce the optimal V/V_{max} for producing power [43]. However, recent work demonstrates that muscle contractions beginning at longer starting lengths (stretched slightly beyond optimal length) enable the muscle to reach the plateau of the F–L curve at the time of maximum muscle activation [22]. Thus, at the time point of peak activation and muscle power, F–L effects would not influence maximum muscle power for the current model. Indeed, our *in silico-robotic* experiments, which do include F–L effects, match well with our simple model predictions (figure 6).

Secondly, experiments were performed in still water without translational motion of the foot. In a simple rower (figure 2*d*), oar blades would have an aft-directed rotational and translational component as they rotate about their base. Therefore, in a tethered animal, the oar would 'slip' backward. However if untethered, the body moves forward with respect to the water, whereas the blade moves backward with respect to the body. As a result, an oar's backwards translation is cancelled by forward swimming such that the motion of the oar base is nearly fixed in the global reference frame, as evident in swimming insects [20], aquatic frogs [8,15] and in human-powered rowing [44]. In these cases, we capture important aspects of muscle–fluid dynamics in the absence of modelling forward body motion. In cases where rowing appendages are thrust backwards (e.g. ranid frogs [10]), our model is less accurate. In either forward or backward translation cases, our simple model would overestimate outlever (R) length as the fluid reaction force vector deviates from normal to the foot surface [8]. Consequently for large foot sizes which cause large fluid forces and faster swimming speeds, our simple model would overestimate GR. For our current results, such an overestimation would shift our estimates of *in vivo* GR rightward (away from the predicted optimum for ranids and towards the optimum for *X. laevis*; figure 3*b*). Thus, in cases of fast forward swimming (e.g. the second or third kick when the foot rotates as the body is already in motion) or in rapid backward translation (common in ranids), one must quantify translational and rotational velocity components to account for the deflection of the fluid reaction force vector [8]. In addition, the current simple analytical model is not appropriate for acceleration-based swimming. In cases when limb accelerations are extreme and fluid dynamic loads are dominated by the acceleration reaction (e.g. very small frogs [8] or suction feeding fish [45]), our model does not apply because the coupling between shortening velocity and fluid drag would be relatively unimportant. Finally, we address time-varying gearing. Although inlever (r) does not vary over the *in vivo* range of frog ankle joint motion [27,30,31], the outlever (R) may vary due to (i) the angle of the fluid reaction force vector changing with respect to the foot orientation [8] or (ii) as the foot's position relative to the ankle changes throughout a stroke. To address this, R can be estimated at various points in the foot stroke (see §2).

4.6. Summary

We present an approach which may be used to predict muscle performance during swimming using morphological (GR, foot area) and physiological (V_{max}, F_{max}) constants. We found that *X. laevis* hindlimbs possess morphology that is appropriate given muscle intrinsic properties and PCSA. Such 'tuning' of morphological and physiological properties probably enable the muscle to shorten near $1/3V_{max}$ to approach maximal power during swimming.

More generally, the current study addresses dilemmas that arise when limb morphology is considered without regard to underlying muscle properties (and *vice versa*). Based on fin area alone, one might falsely conclude that ranid frogs produce lower power outputs in fluid than aquatic frogs which possess larger feet. However, based on the larger PCSA of ranids compared with *X. laevis*, one might reach the opposite conclusion. We resolve such dilemmas with a model that predicts functional relationships among morphological and physiological properties. Perhaps our simple approach can be used to suggest pathways by which natural selection influences performance through the modification of either muscle or limb properties.

Firstly, we thank Andrew Carroll for discussions prior to the onset of this work that stimulated our interest in the coupling of fluid drag and muscle force–velocity effects. We thank Henry Astley for helpful advice regarding force–velocity experiments. We thank Tom Roberts for his suggestion to investigate temperature effects of V_{max}. In addition, we are thankful for informative discussions with Jim Dreher, Coleen Fuerst and Linda Stern regarding the mechanics of human rowing. This work was supported by the Rowland Jr. Fellows programme at the Rowland Institute at Harvard.

References

1. Rand SA. 1952 Jumping ability of certain anurans, with notes on endurance. *Copeia* **1952**, 15–20. (doi:10.2307/1437615)
2. Zug GR. 1978 Anuran locomotion—structure and function, 2: jumping performance of semiaquatic, terrestrial and arboreal frogs. *Smithsonian contrib. Zool.* **276**, 1–30. (doi:10.5479/si.00810282.276)
3. Lutz GJ, Rome LC. 1994 Built for jumping: the design of the frog muscular system. *Science* **263**, 370–372. (doi:10.1126/science.8278808)
4. Roberts TJ, Marsh RL. 2003 Probing the limits to muscle-powered accelerations: lessons from jumping bullfrogs. *J. Exp. Biol.* **206**, 2567–2580. (doi:10.1242/jeb.00452)
5. Howard WE. 1950 Birds as bullfrog food. *Copeia* **1950**, 152. (doi:10.2307/1438964)
6. Altevogt R, Holtmann H, Kaschek N. 1986 High frequency cinematography studies on locomotion and preying in Indian skitter frogs *Rana cyanophlyctis*. *J. Bombay Nat. Hist. Soc.* **83**, 102–111.
7. Nauwelaerts S, Scholliers J, Aerts P. 2004 A functional analysis of how frogs jump out of water. *Biol. J. Linn. Soc.* **83**, 413–420. (doi:10.1111/j.1095-8312.2004.00403.x)
8. Gal JM, Blake RW. 1988 Biomechanics of frog swimming. I. Estimation of the propulsive force generated by *Hymenochirus boettgeri*. *J. Exp. Biol.* **138**, 399–411.
9. Johansson LC, Lauder GV. 2004 Hydrodynamics of surface swimming in leopard frogs (*Rana pipiens*). *J. Exp. Biol.* **207**, 3945–3958. (doi:10.1242/jeb.01258)
10. Nauwelaerts S, Stamhuis EJ, Aerts P. 2005 Propulsive force calculations in swimming frogs I. A momentum-impulse approach. *J. Exp. Biol.* **208**, 1435–1443. (doi:10.1242/jeb.01509)
11. Gordon AM, Huxley AF, Julian FJ. 1966 The variation in isometric tension with sarcomere length in vertebrate muscle fibres. *J. Physiol.* **184**, 170–192.
12. Hill AV. 1938 The heat of shortening and the dynamic constants of muscle. *Proc. R. Soc. Lond. B* **126**, 136–195. (doi:10.1098/rspb.1938.0050)
13. Daniel T, Jordan C, Grunbaum D. 1992 Hydromechanics of swimming. *Adv. Comp. Environ. Physiol.* **11**, 17–49. (doi:10.1007/978-3-642-76693-0_2)
14. Lafferty KD, Page CJ. 1997 Predation on the endangered tidewater goby, *Eucyclogobius newberryi*, by the introduced African clawed frog, *Xenopus laevis*, with notes on the frog's parasites. *Copeia* **1997**, 589–592. (doi:10.2307/1447564)
15. Richards CT. 2008 The kinematic determinants of anuran swimming performance: an inverse and forward dynamics approach. *J. Exp. Biol.* **211**, 3181–3194. (doi:10.1242/jeb.019844)
16. Lieber RL. 1992 *Skeletal muscle structure and function*. Baltimore, MD: Lippincott Williams & Wilkins.
17. Biewener A. 2003 *Animal locomotion*. Oxford, UK: Oxford University Press.
18. Richards CT, Clemente CJ. 2012 A bio-robotic platform for integrating internal and external mechanics during muscle-powered swimming. *Bioinspir. Biomim.* **7**, 016010. (doi:10.1088/1748-3182/7/1/016010)
19. Aerts P, Nauwelaerts S. 2009 Environmentally induced mechanical feedback in locomotion: frog performance as a model. *J. Theor. Biol.* **261**, 372–378. (doi:10.1016/j.jtbi.2009.07.042)
20. Daniel TL. 1995 Invertebrate swimming: integrating internal and external mechanics. *Symp. Soc. Exp. Biol.* **49**, 61–89.
21. Azizi E, Roberts TJ. 2010 Muscle performance during frog jumping: influence of elasticity on muscle operating lenghts. *Proc. R. Soc. B* **277**, 1523–1530. (doi:10.1098/rspb.2009.2051)
22. Clemente CJ, Richards C. 2012 Determining the influence of muscle operating length on muscle performance during frog swimming using a bio-robotic model. *Bioinspir. Biomim.* **7**, 036018. (doi:10.1088/1748-3182/7/3/036018)
23. Richards CT. 2011 Building a robotic link between muscle dynamics and hydrodynamics. *J. Exp. Biol.* **214**, 2381–2389. (doi:10.1242/jeb.056671)
24. Otten E. 1987 A myocybernetic model of the jaw system of the rat. *J. Neurosci. Methods* **21**, 287–302. (doi:10.1016/0165-0270(87)90123-3)
25. Lee SSM, de Boef Miara M, Arnold AS, Biewener AA, Wakeling JM. 2011 EMG analysis tuned for determining the timing and level of activation in different motor units. *J. Electromyogr. Kinesiol.* **4**, 557–565. (doi:10.1016/j.jelekin.2011.04.003)
26. Moore JH. 1995 Artificial intelligence programming with LabVIEW: genetic algorithms for instrumentation control and optimization. *Comput. Methods Programs Biomed.* **47**, 73–79. (doi:10.1016/0169-2607(95)01630-C)
27. Clemente CJ, Richards CT. Submitted. Muscle function and hydrodynamics limit power and speed in swimming frogs.
28. Richards CT, Biewener AA. 2007 Modulation of *in vivo* muscle power output during swimming in the African clawed frog (*Xenopus laevis*). *J. Exp. Biol.* **210**, 3147–3159. (doi:10.1242/jeb.005207)
29. Kargo WK, Rome LC. 2002 Functional morphology of proximal hindlimb muscles in the frog *Rana pipiens*. *J. Exp. Biol.* **205**, 1987–2004.
30. Lieber RL, Brown CG. 1992 Sarcomere length–joint angle relationships of seven frog hindlimb muscles. *Acta Anat.* **145**, 289–295. (doi:10.1159/000147380)
31. Astley HC, Roberts TJ. 2011 Evidence for a vertebrate catapult: elastic energy storage in the plantaris tendon during frog jumping. *Biol. Lett.* **8**, 386–389. (doi:10.1098/rsbl.2011.0982)
32. Josephson R. 1985 The mechanical power output from striated muscle during cyclic contraction. *J. Exp. Biol.* **114**, 493–512.
33. Altringham JD, Johnston IA. 1990 Scaling effects on muscle function: power output of isolated fish muscle fibers performing oscillatory work. *J. Exp. Biol.* **151**, 453–467.
34. Tu MS, Daniel TL. 2004 Submaximal power output from the dorsolongitudinal flight muscles of the hawkmoth *Manduca sexta*. *J. Exp. Biol.* **207**, 4651–4662. (doi:10.1242/jeb.01321)
35. Emerson SB. 1982 Frog postcranial morphology: identification of a functional complex. *Copeia* **1982**, 603–613. (doi:10.2307/1444660)
36. Nauwelaerts S, Ramsay J, Aerts P. 2007 Morphological correlates of aquatic and terrestrial locomotion in a semi-aquatic frog, *Rana esculenta*: no evidence for a design conflict. *J. Anat.* **210**, 304–317. (doi:10.1111/j.1469-7580.2007.00691.x)
37. Richards CT. 2010 Kinematics and hydrodynamics analysis of swimming anurans reveals striking inter-specific differences in the mechanism for producing thrust. *J. Exp. Biol.* **213**, 621–634. (doi:10.1242/jeb.032631)
38. Galantis A, Woledge RC. 2003 The theoretical limits to the power output of a muscle–tendon complex with inertial and gravitational loads. *Proc. R. Soc. Lond. B* **270**, 1493. (doi:10.1098/rspb.2003.2403)
39. Herrel A, Bonneaud C. 2012 Trade-offs between burst performance and maximal exertion capacity in a wild amphibian, *Xenopus tropicalis*. *J. Exp. Biol.* **215**, 3106–3111. (doi:10.1242/jeb.072090)
40. Marsh R. 1994 Jumping ability of anuran amphibians. *Adv. Vet. Sci. Comp. Med.* **38**, 51–111.
41. Western Regional Climate Center. 2012 *Western regional climate center*. Reno, NV, USA. See http://www.wrcc.dri.edu/.
42. Nelson FE, Gabaldón AM, Roberts TJ. 2004 Force–velocity properties of two avian hindlimb muscles. *Comp. Biochem. Physiol. A Mol. Integr. Physiol.* **137**, 711–721. (doi:10.1016/j.cbpb.2004.02.004)
43. Askew GN, Marsh RL. 1998 Optimal shortening velocity (V/V_{max}) of skeletal muscle during cyclical contractions: length–force effects and velocity-dependent activation and deactivation. *J. Exp. Biol.* **201**, 1527–1540.
44. Macrossan MN. 2008 The direction of the water force on a rowing blade and its effect on efficiency. Mechanical Engineering report 3. The University of Queensland, St Lucia QLD, Australia.
45. Van Wassenbergh S, Strother JA, Flammang BE, Ferry-Graham LA, Aerts P. 2008 Extremely fast prey capture in pipefish is powered by elastic recoil. *J. R. Soc. Interface* **5**, 285–296. (doi:10.1098/rsif.2007.1124)